

Effect of transition metal substitution on elastoplastic properties of LiMn_2O_4 spinel

Frank P. McGrogan¹ · Yet-Ming Chiang¹ · Krystyn J. Van Vliet¹

Received: 16 August 2016 / Accepted: 14 November 2016 / Published online: 24 November 2016
© Springer Science+Business Media New York 2016

Abstract LiMn_2O_4 (LMO) derivatives partially substituted with transition metals (e.g., Ni) have received attention for their higher energy density achieved at higher charge voltage than pure LMO, and may be attractive cathode candidates for emerging all solid state batteries. Accurate mechanical properties of these high voltage spinels are required for prediction of electrode and electrolyte fracture that may compromise battery lifetime and performance. Here, we quantified the Young's elastic modulus E and hardness H for LMO, $\text{LiMn}_{1.5}\text{Ni}_{0.5}\text{O}_4$ (LMNO), and $\text{LiMn}_{1.5}\text{Ni}_{0.42}\text{Fe}_{0.08}\text{O}_4$ (LMNFO) spinel microparticles via instrumented grid nanoindentation. Elastic modulus E and hardness H increased by more than 40% (up to 145 and 11 GPa, respectively) as a result of Ni or Ni/Fe substitution; such substitution also reduces the lattice parameter and increases the oxidation state of Mn. These results demonstrate how changes in transition metal occupancy can significantly affect the mechanical properties of LMO spinel, and provide critical parameters for designing against fracture in all solid state batteries.

Keywords High-voltage cathodes · Spinel cathodes · Battery mechanics · Nanoindentation · All solid state batteries · Electrochemomechanics

Electronic supplementary material The online version of this article (doi:10.1007/s10832-016-0057-7) contains supplementary material, which is available to authorized users.

✉ Krystyn J. Van Vliet
krystyn@mit.edu

¹ Department of Materials Science & Engineering, Massachusetts Institute of Technology, Cambridge, MA 02139, USA

1 Introduction

All solid state Li-ion batteries are predicted to enable energy-dense electrodes that otherwise face challenges in conventional batteries with liquid electrolytes [1, 2]. For example, $\text{LiMn}_{1.5}\text{Ni}_{0.5}\text{O}_4$ (LMNO) exhibits an operating voltage around 4.7 V with respect to Li^0 , leading to oxidation of typical organic liquid electrolytes at the cathode and limiting the commercial use of LMNO [3, 4]. This electrolyte stability issue is potentially avoided in all solid state batteries, for which the side reactions may be kinetically stifled [5, 6]. Furthermore, the use of a solid electrolyte is expected to reduce Li dendrite growth, common for Li metal anodes used with liquid electrolytes or graphite anodes at high charge rates. The high energy density offered by high-voltage cathodes such as LMNO may thereby be more fully realized in an all solid state battery.

However, the mechanical compatibility constraints inherent to solid state batteries will likely pose a series of new challenges. The concurrent volume changes of positive and negative electrodes during electrochemical cycling, by chemical expansion (~7 vol% for LMO [7, 8]) or by electroplating for a Li anode, can produce significant strains that must be accommodated within the electroactive “stack” [9]. Resulting fracture in the electrolyte or at the electrode-electrolyte interface can disrupt Li ion flow and provide pathways for dendritic growth of Li. Likewise, fracture of the electrode materials, termed “electrochemical shock,” may result from stress build-up within the particles [10–12]. Such fracture is thought to diminish electrode performance in conventional batteries with liquid electrolytes by accelerating active material dissolution, consuming working Li by continued formation of the solid-electrolyte interphase, or slowing Li-ion diffusion within the active material [13–15]. The prevention of fracture during repeated cycling is therefore of great importance for

maximizing the lifetime of both conventional and all solid state batteries, and a critical step in modeling and predicting this fracture is to quantify the elastic and plastic mechanical behavior of the electrode compounds.

In this study, we investigated the mechanical behavior of LiMn_2O_4 (LMO), LMNO, and $\text{LiMn}_{1.5}\text{Ni}_{0.42}\text{Fe}_{0.08}\text{O}_4$ (LMNFO) cathodes. LMNO crystallizes in the cubic spinel structure, like LMO, but has 1 in 4 of the Mn atoms on the 16d sublattice replaced with Ni [16–18]. The introduction of Ni increases the average oxidation state of Mn to 4+, eliminating the $\text{Mn}^{3+/4+}$ redox couple at 4.0 V and replacing it with $\text{Ni}^{2+/4+}$ at 4.7 V. In batteries using liquid electrolytes, the persisting issue of transition metal dissolution into the electrolyte prompted investigations of further doping with additional metals such as Fe and Co [19–22]. As discussed by others [11, 17, 21], the addition of small amounts of Fe to produce LMNFO improves the surface chemistry of the spinel, mitigates phase transformations responsible for particle fracture [11], and improves Li^+ diffusivity. As most of these advantages of LMNFO also apply to all solid state batteries, in this study we chose to compare this compound to LMO and LMNO.

Although to our knowledge the Young's elastic modulus E and hardness H for LMNO and LMNFO have not been characterized previously, the mechanical properties of LMO have been reported extensively in the literature and serve as a useful reference. For LMO, E has been quantified by pressure-controlled X-ray diffraction (XRD) [23, 24], the vibrating reed technique [25, 26], and computation [27–29]. Those studies have yielded numerical values spanning more than an order of magnitude. E and H of LMO have also been measured by nanoindentation for both particles and thin films [30–32], including the effects of delithiation on these properties [31]. Fracture toughness K_{Ic} of LMO was measured by Mughal et al. via a focused ion beam technique [33]. Here, we used instrumented nanoindentation to measure E and H in the LMO spinel family of cathode materials, analyzing mechanical responses of individual cathode microparticles within a mechanically defined matrix. For undoped, stoichiometric LMO, E of 100 ± 8 GPa and H of 7.5 ± 0.9 GPa agree well with prior nanoindentation studies [30, 31]. For LMNO, E and H increased to 136 ± 12 GPa and 10.1 ± 1.9 GPa, respectively. The qualitative trend is consistent with the lattice parameter reduction occurring upon an increase in the $\text{Mn}^{4+}/\text{Mn}^{3+}$ ratio [19]. Finally, for LMNFO containing 0.08 Fe per formula unit, E and H were 145 ± 15 GPa and 11.0 ± 1.8 GPa, respectively, indicating a small increase in elastoplastic properties as compared with LMNO. Thus, up to 40% resistance to reversible deformation (elastic modulus) and 40% resistance to permanent deformation and flow (hardening) are induced by 25 at.% substitution of Ni for Mn. These findings establish baseline values for the mechanical properties of the fully lithiated compositions of these spinels.

2 Experimental

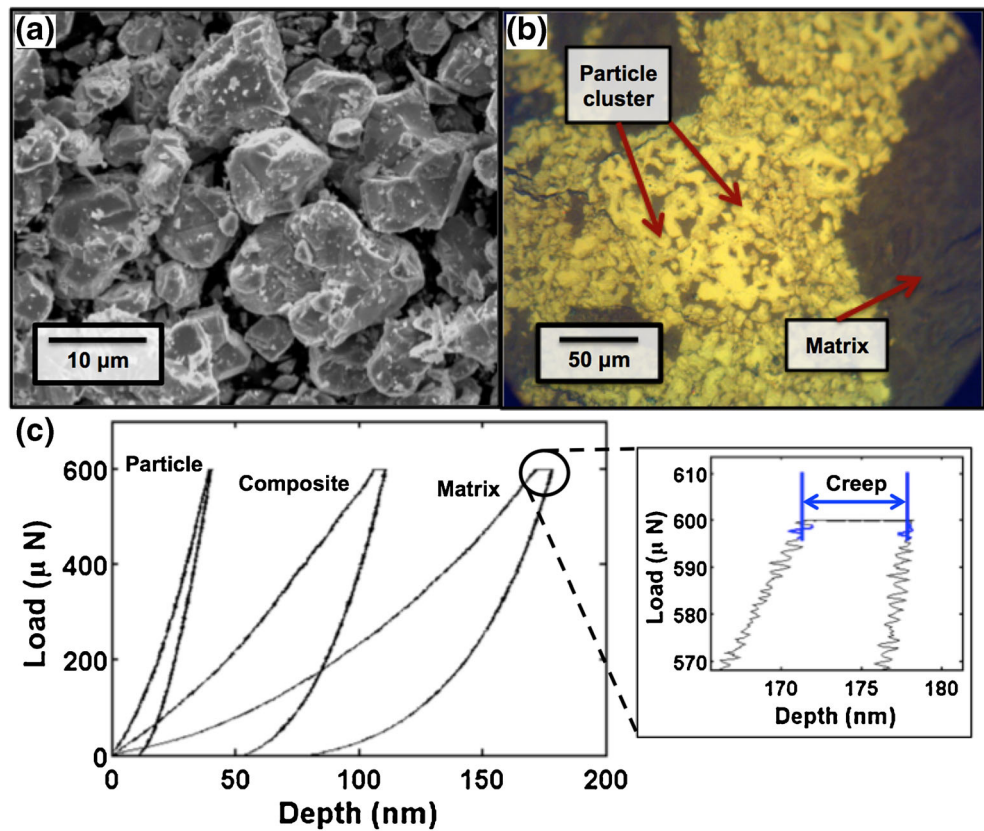
2.1 Sample preparation

Commercial LMO powder (Toda Kogyo Corp., Japan) was used for LMO samples, with a primary crystallite diameter of 1–2 μm as characterized by scanning electron microscopy (XL30 ESEM, FEI, Hillsboro, OR). Powders of LMNO and LMNFO were prepared by ball milling stoichiometric amounts of LiCO_3 , Mn_2O_3 , NiO, and Fe_3O_4 in acetone for 24 h, pouring the slurry onto Al foil to dry, and calcining the dried product for 12 h at 900°C in air [11]. Samples were then ground by hand in a mortar and pestle and analyzed via XRD (PANalytical X'Pert Pro diffractometer) to verify the identity of the powder, as discussed in the Supplementary Material. To minimize the effect of finite particle dimensions in the indentation experiments [34–36], all samples were uniaxially pressed into pellets for 2 min at 140 MPa and coarsened at 950°C in 12–24 h segments to attain an abundance of particles of diameters of 8–10 μm (see Fig. 1a). Additional coarsening treatments yielded diminishing returns in increasing particle diameter. The powder was ground and re-pressed between each coarsening step.

Sintering to achieve 50–100 μm grain size and fully dense compacts was not possible for LMO and its derivatives, though previously demonstrated by us for LiCoO_2 (LCO) powder [37, 38]. Thus, each spinel powder sample was mixed with a thermosetting phenol formaldehyde resin matrix (Bakelite) to enable direct mechanical testing of microscale spinel particles within a well-defined composite. The mixed powder of resin and spinel of a given composition was formed into a disk of diameter 3.2 cm via hot mounting at 155°C and ~ 32 MPa, then cooled to room temperature. The resulting composite was polished to provide a flat testing surface using SiC sandpaper of decreasing grits (800, 1200, 2400, 4000) with water lubrication, and diamond polishing pads (UltraPrep, Buehler Limited, Lake Bluff, IL) of 3 μm , 1 μm and 0.5 μm grit sizes with no additional lubrication. Samples were rinsed with water between each polishing step. Figure 1(b) illustrates representative clusters of agglomerated LMO particles in the thermoset matrix after polishing. Before mechanical characterization, samples were adhered to a steel plate with low-viscosity cyanoacrylate for magnetic sample mounting on the indentation stage.

A reference sample of LCO particles was also prepared for mechanical characterization. A dense compact was produced by pressing, sintering, and coarsening as described previously [38], then crushed with a mortar and pestle into a powder. The size similarity between the coarsened grains and resulting particles post-grinding suggested that the grains of the sintered compact became the loose particles upon grinding. Although some LCO particles exceeded the size of the LMO-based spinel particles, as quantified by optical microscopy, a subset of

Fig. 1 (a) Scanning electron micrograph of synthesized $\text{LiMn}_{1.5}\text{Ni}_{0.42}\text{Fe}_{0.08}\text{O}_4$ particles after high-temperature coarsening treatments. Particle diameter ranged 8–10 μm . (b) Coarsened LiMn_2O_4 embedded in thermoset matrix and polished. (c) Representative load-depth curves acquired via load-controlled nanoindentation exhibiting particle-dominated, matrix-dominated, and composite responses. Maximum indentation depth and extent of viscoelastic behavior both increase with matrix influence



LCO particles was of the desired diameter of 8–10 μm . The LCO powder was mixed with thermoset resin powder, heated, polished, and mounted using the same procedure as was used for the spinel powders. For LCO, E and H have been established previously by Qu et al. [37] on dense sintered compacts comprising $\sim 100 \mu\text{m}$ grain diameters (and thus no mounting matrix), as discussed in the Supplementary Material.

2.2 Nanomechanical characterization

Mechanical properties E and H were obtained by carrying out instrumented nanoindentation (Hysitron, Inc. Triboindenter, Minneapolis, MN) in grid patterns over the ceramic/polymer composite surface using a diamond Berkovich probe. This method has been validated previously by us and others for natural and engineered composites [39, 40], and was further validated in the present study via testing of the LCO particle reference sample; see Supplementary Material.

Indentation grids on the spinel samples were acquired over regions composed of many particles of $\sim 10 \mu\text{m}$ diameter as in Fig. 1(b), selected via optical microscopy within the instrumented indenter. These grids were selected to maximize the degree of particle phase encountered by the indentations, but a mixture of particle- and matrix-dominated measurements was expected. The thermoset polymeric resin matrix exhibited

lower E (~ 10 GPa, also measured via indentation); this was known to be lower than that expected of metal oxide materials. This matrix was chosen to enable secure particle mounting and polishing as required for indentation without significant spinel sample manipulation with temperature or chemicals. This mechanical contrast between the metal oxide particles and the polymer matrix also facilitated statistical clustering to distinguish particle-dominated and matrix-dominated mechanical responses.

As shown in Fig. 1(c), the P - h (load-depth) responses for particle- and matrix-dominated measurements are distinguishable qualitatively by the steepness of the loading profile, maximum depth h_{max} , and extent of creep occurring at h_{max} . For the reference LCO sample, groups of particles with particle size 8–10 μm were targeted for comparison with the spinel samples of similar particle diameter. Indentation centers within each grid were spaced by 6–8 μm for all samples, and maximum load of 600 μN was achieved at a constant loading rate over 10 s, followed by holding at maximum load for 3 s and unloading over another 10 s. For LMO, indentations were also conducted at 1200 μN , 1800 μN , and 2400 μN to investigate whether the indentations occurred in a regime where the measured elastic modulus was sensitive to the ratio of maximum depth to particle radius h_{max}/R as discussed by Yan et al. [36] Although load-independence was observed for LMO as discussed below and in the Supplementary Material, we

conservatively applied the lowest maximum load (600 μN) to maximize data acquisition dominated by particle contributions. This range of maximum loads resulted in maximum depths within the spinel particles of 30–120 nm.

A fused quartz sample was used to calibrate machine compliance and indenter probe geometry (area function), including calibrations at maximum depths (30–120 nm) typically achieved in the spinel particles.

2.3 Nanomechanical data analysis

Mechanical data were analyzed in two steps. First, the Young's elastic modulus E and hardness H were calculated for each load-depth profile as described below, according to established and automated methods. Second, these data were analyzed via clustering algorithms to identify the particle-dominated mechanical responses. This approach was combined with alternative examinations of the data, including cumulative distribution functions (CDFs), to obtain quantitatively consistent results for E and H of each material.

For each load-depth profile acquired, reduced modulus E_r was calculated via the Oliver-Pharr method [41–43], relating the initial unloading response dP/dh to the elastic response:

$$E_r = \frac{\sqrt{\pi}}{2} \frac{1}{\sqrt{A}} \frac{dP}{dh} \quad (1)$$

where P , h , and A correspond to the variables load, displacement, and projected indentation area, respectively. The Young's elastic modulus E of the material sample was calculated from E_r by accounting for the mechanical properties of the diamond indenter:

$$\frac{1}{E_r} = \frac{(1-\nu^2)}{E} + \frac{(1-\nu_i^2)}{E_i} \quad (2)$$

where E_i and Poisson's ratio ν_i of the diamond indenter were taken to be 1070 GPa and 0.07, respectively, and the Poisson's ratio ν of the sample was taken to be 0.3. Hardness was calculated as the ratio of the maximum applied load to the projected indentation contact area at this load:

$$H = \frac{P_{max}}{A} \quad (3)$$

All raw load-depth responses were viewed and recorded, and E_r and H for all samples were calculated by an automated script in the Hysitron software according to the Oliver-Pharr method. Afterward, several grids of E data were superimposed on images obtained with the Hysitron optics to confirm spatial correlation between particle phase and high E measurement.

In applying principal component analysis (PCA) to distinguish particle-dominated from matrix-dominated indentation responses, we selected three important characteristics to

define each measurement: computed E , computed H , and creep displacement. Creep displacement was defined for each P - h profile by the total displacement at maximum load, as indicated in Fig. 1(c). Quadratic fit quality [30] and h_{max} were also considered initially, but reduced the quality of the clustering procedure. The dimensionality of the data was then reduced from 3 to 2 by the "pca" procedure in MATLAB, with which two axes are selected to display the data in the directions of highest variance, or principal components. The new axes of the data are linear combinations of the original 3 axes. The resulting data displayed on a 2-axis plot were then grouped into clusters using the "kmeans" algorithm in MATLAB.

All mechanical property data are reported as mean \pm standard deviation. When comparing means obtained with different variances and sample sizes n , Welch's t -test was used to identify differences with statistical significance.

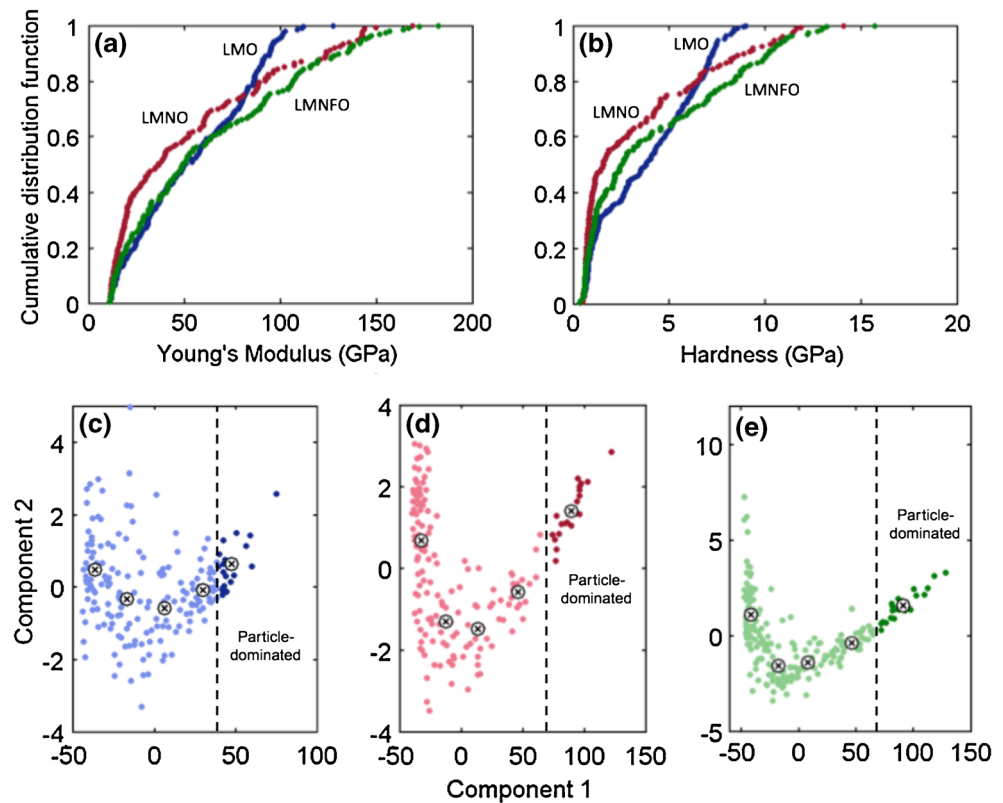
3 Results and discussion

3.1 Distribution of E and H measurements with particle and matrix influence

Due to the finite particle size and a large difference between particle and matrix stiffness, the cumulative distribution functions (CDFs) shown in Fig. 2(a-b) indicate a wide range of measured E and H . The measurements varied continuously between the particle and matrix modulus endpoints without exhibiting distinct regions belonging to each phase, suggesting that the majority of measurements are influenced by both the matrix and particle phases. However, despite an apparent scarcity of pure particle measurements, a qualitative difference in mechanical behavior is clear between the Ni/Fe substituted spinels and pure LMO samples. For both E and H , the measurements for LMNO and LMNFO tended toward significantly higher particle-dominated endpoints, indicating an increase in E and H for these spinels as compared with LMO.

Multiple analyses were used to ascertain that the qualitative increases in E and H in Fig. 2(a-b) were not caused by inconsistent sampling errors, such as unequal particle size distributions or overly high indentation loads. As shown in the Supplementary Material, E and H indentation grids were acquired for the LMO sample at 600, 1200, 1800, and 2400 μN loading, and the corresponding CDFs converge at both the low and high ends of the measured E spectrum. The consistency of the CDFs indicates that the sensitivity to peak load and h_{max}/R is low in this load range. Furthermore, the agreement of E in the high-modulus range at all peak loads indicates that the data do indeed converge to the elastic modulus of LMO. Further confirmation of the observed trend can be obtained by viewing the data trends in E vs. h_{max} format, creep displacement vs. h_{max} format, and by comparing the CDFs to

Fig. 2 Cumulative distribution functions for (a) Young's modulus and (b) hardness of all spinel samples. Young's modulus, hardness and creep displacement data for (c) LiMn_2O_4 , (d) $\text{LiMn}_{1.5}\text{Ni}_{0.5}\text{O}_4$, and (e) $\text{LiMn}_{1.5}\text{Ni}_{0.42}\text{Fe}_{0.08}\text{O}_4$ are shown in a 2-dimensional space determined by principal component analysis. Clusters assigned to particle-dominated measurements are highlighted



the reference LCO sample. These analyses are detailed in the Supplementary Material.

3.2 Selection of particle-dominated measurements for quantification of E and H

Although the experiments discussed above demonstrate that the particle-dominated regime is accessible in our measurements, quantification of E and H for the LMO-based phases from these spectra required further treatment of the data. As no discontinuity is apparent in our CDFs, the data do not lend themselves to visually obvious, objective separation between matrix- and particle-dominated measurements. Therefore, we used a principal component analysis (PCA) and clustering technique to identify the designated particle-dominated measurements for each sample. PCA included computed E , computed H , and creep displacement as described in Methods.

Figure 2(c–e) shows the indentations of each sample in the optimized component space, with particle-dominated measurements clustered at higher magnitudes of “component 1” as indicated by the dashed verticals. We also conducted sensitivity tests to vary the number of clusters k between 3 and 7 until the particle-dominated cluster was invariant with further cluster additions. At $k = 5$ for all samples, a cluster was consistently identified in a region of high data density at the particle-dominated extreme of the data. The members of these clusters exhibit the expected qualitative features of the particle

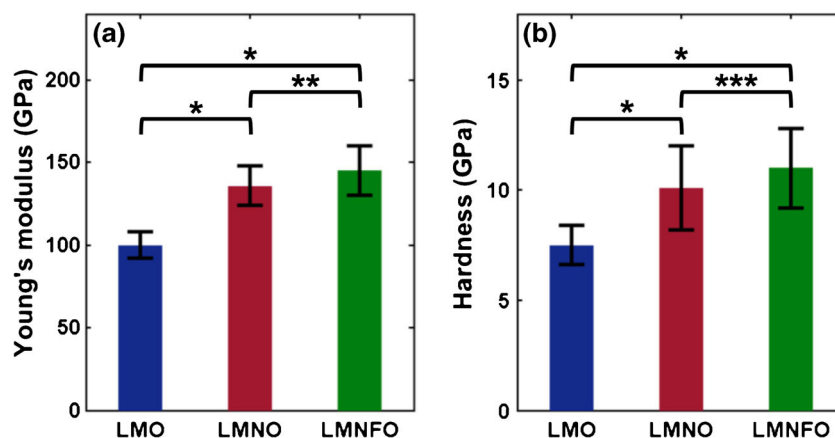
phase – high E , high H , and low creep displacement (as compared with the other data points within that sample set). Although this method is useful for defining groups at the extreme of each data set, the grouping of the data into five clusters does not have physical meaning. Only two phases exist, with a range of measurements between them, and the clustering at the data extremes is caused by the convergence of data to the particle and matrix limits. Details of the k sensitivity test are discussed further in the Supplementary Material.

3.3 Comparison of samples based on particle-dominated measurements

The selected particle-dominated groups were used to compute E and H for each sample, and these results are shown in both Fig. 3 and Table 1, where n is the number of independent indentation experiments represented within the particle-dominated cluster for each material. From these results, it is clear that both the elastic modulus and hardness of the Ni and Ni/Fe substituted derivatives were significantly higher than those of LiMn_2O_4 . This comparison confers a high degree of statistical significance ($p < 0.0001$, Welch's t-test), and represents an approximately 40% increase in stiffness and hardness upon substitution with Ni to form either LMNO or LMNFO of these compositions.

This increase of E and H upon Ni substitution within LiMn_2O_4 is consistent with the change in lattice parameter

Fig. 3 Young's modulus and hardness for LiMn_2O_4 (LMO), $\text{LiMn}_{1.5}\text{Ni}_{0.5}\text{O}_4$ (LMNO), and $\text{LiMn}_{1.5}\text{Ni}_{0.42}\text{Fe}_{0.08}\text{O}_4$ (LMNFO). Error bars are standard deviations. Asterisks denote statistical significance: $p < 0.0001$ (*), $p \sim 0.03$ (**), and $p \sim 0.14$ (***)



and $\text{Mn}^{4+}/\text{Mn}^{3+}$ ratio. Amanieu et al. [31] observed an increase in E and H due to delithiation of pure LMO, which was attributed to increased Mn-O bond strength upon Mn^{3+} oxidation to Mn^{4+} and marked by a corresponding decrease in lattice parameter [44]. Likewise, the inclusion of Ni to form $\text{LiMn}_{1.5}\text{Ni}_{0.5}\text{O}_4$ causes Mn to be fully oxidized to Mn^{4+} and results in a decreased lattice parameter [19, 45]. Importantly, the increased stiffness and hardness of this candidate battery electrode material upon Ni doping indicates lower capability to accommodate strain in an all solid state battery, as well as increased elastic stress fields contributing to fracture within the electrode material for both conventional and all solid state applications [10, 12, 46, 47].

Additionally, elastic modulus increased slightly as a result of Fe doping: mean E of LMNFO was 7% higher than that of LMNO. This effect, though statistically significant ($p \sim 0.03$), represented a mildly increased stiffness of only 9 GPa for a partial doping of Fe on the Mn and Ni sites as indicated by $\text{LiMn}_{1.5}\text{Ni}_{0.42}\text{Fe}_{0.08}\text{O}_4$. The hardness of the Fe-doped spinel was not statistically different from its Ni-substituted counterpart LMNO ($p \sim 0.14$). The physical basis by which Fe doping can further stiffen the spinel requires further study, though we note that experimental and computational studies of other complex metal oxides have attributed detectable changes in E to lattice parameter changes associated with electronic and point defects [48]. By the same reasoning that LMNO should display higher E and H than LMO, the inclusion of Fe in LMNO lowers the Mn oxidation state and increases the lattice parameter [19], suggesting that at sufficient Fe doping the E and H for LMNFO be intermediate to that of LMO and

LMNO. Despite apparently higher E , the propensity for electrochemical shock has been shown to decrease in LMNFO, but this has been attributed to reduction of phase transformation strain via modification of the phase diagram [11, 21].

Although it is possible in principle for powder processing and particle morphology to contribute to such mechanical differences, we maintained particle coarsening and treatment conditions uniform among samples and found all spinel materials to exhibit indistinguishable particle morphology and size (see Supplementary Material). Thus, our findings indicate that Ni substitution of LiMn_2O_4 significantly and substantially increases the stiffness and hardness of this spinel candidate for active electrode materials in all solid state batteries, in the form of $\text{LiMn}_{1.5}\text{Ni}_{0.5}\text{O}_4$ or $\text{LiMn}_{1.5}\text{Ni}_{0.42}\text{Fe}_{0.08}\text{O}_4$. Additional doping of Fe in a Ni substituted LMO derivative mildly increases stiffness but not hardness, and thus more detailed computational studies may elucidate how additional or different transition metals can affect these elastoplastic properties of LMNO.

4 Conclusions

We report the first measurements of two key mechanical properties for LMNO and LMNFO spinels, elastic modulus relating to reversible deformation and hardness relating to plastic flow. Grid arrays of nanoindentation on spinel microparticles embedded in a polymer matrix provided E and H over a range of composite responses spanning from the matrix-dominated to particle-dominated regimes. PCA and two-dimensional clustering facilitated objective identification of particle-dominated measurements. From those data, we determine that E and H increase by $\sim 40\%$ upon Ni and Ni/Fe doping as compared to LMO, up to as much as 145 GPa and 11.0 GPa, respectively. These results demonstrate how the stiffness and resistance to permanent deformation of the manganese spinel family of cathodes is influenced by transition metal substitution on the 16d sites, and enable further

Table 1. Young's modulus E and hardness H for LiMn_2O_4 and its Ni/Fe substituted derivatives

Material	E (GPa)	H (GPa)	n of cluster
LiMn_2O_4	100 ± 8	7.5 ± 0.9	23
$\text{LiMn}_{1.5}\text{Ni}_{0.5}\text{O}_4$	136 ± 12	10.1 ± 1.9	19
$\text{LiMn}_{1.5}\text{Ni}_{0.42}\text{Fe}_{0.08}\text{O}_4$	145 ± 15	11.0 ± 1.8	23

investigations on the effects of stress distributions and fracture criteria for both conventional and all solid state battery systems.

Acknowledgements We gratefully acknowledge support from the US Department of Energy's Office of Basic Energy Science for the Chemomechanics of Far-From-Equilibrium Interfaces (COFFEI) small group, through award number DE-SC0002633 (J. Vetrano, Program Manager). We also acknowledge use of the MIT Nanomechanical Technology Laboratory (A. Schwartzman, Manager). This work made use of the Shared Experimental Facilities supported in part by the MRSEC Program of the National Science Foundation under award number DMR-1419807.

Compliance with ethical standards

Conflict of interest The authors declare that they have no conflict of interest.

References

- J. Li, C. Ma, M. Chi, C. Liang, N. J. Dudney, *Adv. Energy Mater.* **5**, 1401408 (2015)
- J. G. Kim, B. Son, S. Mukherjee, N. Schuppert, A. Bates, O. Kwon, M. J. Choi, H. Y. Chung, S. Park, *J. Power Sources* **282**, 299 (2015)
- M. Hu, X. Pang, Z. Zhou, *J. Power Sources* **237**, 229 (2013)
- K. R. Chemelewski, E.-S. Lee, W. Li, A. Manthiram, *Chem. Mater.* **25**, 2890 (2013)
- K. Takada, *Acta Mater.* **61**, 759 (2013)
- Y. Zhu, X. He, Y. Mo, *ACS Appl. Mater. Interfaces* **7**, 23685 (2015)
- X. Q. Yang, X. Sun, S. J. Lee, J. McBreen, S. Mukerjee, M. L. Daroux, X. K. Xing, *Electrochem. Solid-State Lett.* **2**, 157 (1999)
- T. Ohzuku, M. Kitagawa, T. Hirai, *J. Electrochem. Soc.* **137**, 769 (1990)
- S. R. Bishop, D. Marrocchelli, C. Chatzichristodoulou, N. H. Perry, M. B. Mogensen, H. L. Tuller, E. D. Wachsman, *Annu. Rev. Mater. Res.* **44**, 205 (2014)
- W. H. Woodford, Y.-M. Chiang, W. C. Carter, *J. Electrochem. Soc.* **157**, A1052 (2010)
- W. H. Woodford, W. C. Carter, Y.-M. Chiang, *J. Electrochem. Soc.* **161**, F3005 (2014)
- W. H. Woodford, Y.-M. Chiang, W. C. Carter, *J. Electrochem. Soc.* **160**, A1286 (2013)
- J. Vetter, P. Novák, M. R. Wagner, C. Veit, K.-C. Möller, J. O. Besenhard, M. Winter, M. Wohlfahrt-Mehrens, C. Vogler, A. Hammouche, *J. Power Sources* **147**, 269 (2005)
- A. Mukhopadhyay, B. W. Sheldon, *Prog. Mater. Sci.* **63**, 58 (2014)
- R. Narayanrao, M. M. Joglekar, S. Inguva, *J. Electrochem. Soc.* **160**, A125 (2013)
- Q. Zhong, A. Bonakdarpour, M. Zhang, J. R. Dahn, *J. Electrochem. Soc.* **144**, 205 (1997)
- J. Liu, A. Manthiram, *J. Phys. Chem. C* **113**, 15073 (2009)
- A. Manthiram, K. Chemelewski, E.-S. Lee, *Energy Environ. Sci.* **7**, 1339 (2014)
- G. T.-K. Fey, C.-Z. Lu, T. P. Kumar, *J. Power Sources* **115**, 332 (2003)
- D. Aurbach, B. Markovsky, Y. Talyossef, G. Salitra, H.-J. Kim, S. Choi, *J. Power Sources* **162**, 780 (2006)
- T. A. Arunkumar, A. Manthiram, *Electrochem. Solid-State Lett.* **8**, A403 (2005)
- Y. Shin, A. Manthiram, *J. Electrochem. Soc.* **151**, A204 (2004)
- J. Darul, W. Nowicki, P. Piszora, *J. Phys. Chem. C* **116**, 17872 (2012)
- Y. Lin, Y. Yang, H. Ma, Y. Cui, W. L. Mao, *J. Phys. Chem. C* **115**, 9844 (2011)
- J. Sugiyama, T. Tamura, H. Yamauchi, *J. Phys. Condens. Matter* **7**, 9755 (1995)
- A. Paolone, R. Cantelli, G. Rousse, C. Masquelier, *J. Phys. Condens. Matter* **15**, 457 (2003)
- Y. Qi, L. G. Hector Jr., C. James, K. J. Kim, *J. Electrochem. Soc.* **161**, F3010 (2014)
- S. Lee, J. Park, A. M. Sastry, W. Lu, *J. Electrochem. Soc.* **160**, A968 (2013)
- G. E. Grechnev, R. Ahuja, B. Johansson, O. Eriksson, *Phys. Rev. B* **65**, 174408 (2002)
- H.-Y. Amanieu, D. Rosato, M. Sebastiani, F. Massimi, D. C. Lupascu, *Mater. Sci. Eng. A* **593**, 92 (2014)
- H.-Y. Amanieu, M. Aramfard, D. Rosato, L. Batista, U. Rabe, D. C. Lupascu, *Acta Mater.* **89**, 153 (2015)
- K. Zeng, J. Zhu, *Mech. Mater.* **91**, 323 (2015)
- M. Z. Mughal, R. Moscatelli, H.-Y. Amanieu, M. Sebastiani, *Scr. Mater.* **116**, 62 (2016)
- W. Yan, C. L. Pun, G. P. Simon, *Compos. Sci. Technol.* **72**, 1147 (2012)
- J. W. Leggoe, *J. Mater. Res.* **19**, 2437 (2004)
- W. Yan, L. P. Chung, Z. Wu, G. P. Simon, *Compos. Part B* **42**, 2093 (2011)
- M. Qu, W. H. Woodford, J. M. Maloney, W. C. Carter, Y.-M. Chiang, K. J. Van Vliet, *Adv. Energy Mater.* **2**, 940 (2012)
- J. G. Swallow, W. H. Woodford, F. P. McGrogan, N. Ferralis, Y.-M. Chiang, K. J. Van Vliet, *J. Electrochem. Soc.* **161**, F3084 (2014)
- G. Constantinides, K. S. Ravi Chandran, F.-J. Ulm, K. J. Van Vliet, *Mater. Sci. Eng. A* **430**, 189 (2006)
- F.-J. Ulm, M. Vandamme, C. Bobko, J. A. Ortega, K. Tai, C. Ortiz, *J. Am. Ceram. Soc.* **90**, 2677 (2007)
- G. M. Pharr, W. C. Oliver, F. R. Brotzen, *J. Mater. Res.* **7**, 613 (1992)
- W. C. Oliver, G. M. Pharr, *J. Mater. Res.* **19**, 3 (2004)
- W. C. Oliver, G. M. Pharr, *J. Mater. Res.* **7**, 1564 (1992)
- B. Xu, S. Meng, *J. Power Sources* **195**, 4971 (2010)
- J. Xiao, X. Chen, P. V Sushko, M. L. Sushko, L. Kovarik, J. Feng, Z. Deng, J. Zheng, G. L. Graff, Z. Nie, D. Choi, J. Liu, J.-G. Zhang, and M. S. Whittingham, *Adv. Mater.* **24**, 2109 (2012).
- P. Barai, P. P. Mukherjee, *J. Electrochem. Soc.* **161**, F3123 (2014)
- X. Zhang, W. Shyy, A. M. Sastry, *J. Electrochem. Soc.* **154**, A910 (2007)
- J. G. Swallow, J. J. Kim, M. Kabir, J. F. Smith, H. L. Tuller, S. R. Bishop, K. J. Van Vliet, *Acta Mater.* **105**, 16 (2016)